

Multi-scale Cascaded Large-Model for Whole-body ROI Segmentation

Rui Hao, Dayu Tan, *Member, IEEE*, Yansen Su and Chunhou Zheng

Abstract—Organs-at-risk segmentation is critical for ensuring the safety and precision of radiotherapy and surgical procedures. However, existing methods for organs-at-risk image segmentation often suffer from uncertainties and biases in target selection, as well as insufficient model validation experiments, limiting their generality and reliability in practical applications. To address these issues, we propose an innovative cascaded network architecture called the Multi-scale Cascaded Fusing Network (MCFNet), which effectively captures complex multi-scale and multi-resolution features. MCFNet includes a Sharp Extraction Backbone and a Flexible Connection Backbone, which respectively enhance feature extraction in the downsampling and skip-connection stages. This design not only improves segmentation accuracy but also ensures computational efficiency, enabling precise detail capture even in low-resolution images. We conduct experiments using the A6000 GPU on diverse datasets from 671 patients, including 36,131 image-mask pairs across 10 different datasets. MCFNet demonstrates strong robustness, performing consistently well across 10 datasets. Additionally, MCFNet exhibits excellent generalizability, maintaining high accuracy in different clinical scenarios. We also introduce an adaptive loss aggregation strategy to further optimize the model training process, improving both segmentation accuracy and efficiency. Through extensive validation, MCFNet demonstrates superior performance compared to existing methods, providing more reliable image-guided support. Our solution aims to significantly improve the precision and safety of radiotherapy and surgical procedures, advancing personalized treatment. The code has been made available on GitHub: <https://github.com/Henry991115/MCFNet>.

Index Terms—Whole-body ROI segmentation, multi-scale cascaded Large-Model, linear attention transformer, adaptive loss aggregation strategy.

I. INTRODUCTION

MEDICAL image segmentation aims to quickly and accurately separate different tissues, organs, or lesion areas, facilitating clinical applications such as disease analysis, lesion detection, and treatment planning [1], [2]. In the field of medical image analysis, accurately identifying and segmenting malignant tumors is crucial for early cancer diagnosis, treatment planning, and efficacy evaluation. However, malignant

tumors are often complex in shape, vary in size, have blurred boundaries, and are closely connected to surrounding tissues, posing significant challenges for accurate tumor identification and segmentation [3]–[5]. Accurately identifying and locating organs-at-risk (OAR) can help doctors and medical teams plan and execute treatment plans. In radiation therapy, precise identification of OAR can assist doctors in minimizing the impact of treatment on surrounding healthy tissues, thereby reducing adverse effects caused by the treatment [6], [7]. Tumor and OAR segmentation are fundamental to treatment planning in radiation therapy. Tumor segmentation helps doctors determine the target area for accurately aiming the radiation dose. Meanwhile, OAR segmentation allows doctors to identify and protect surrounding healthy tissues, avoiding unnecessary damage during treatment [8], [9].

With the emergence of deep learning models, traditional methods constrained by human, financial, and time costs are gradually being abandoned [10]–[13]. Deep learning-based models can automatically learn features from images and efficiently extract features of complex structures and textures, enabling the identification of ROI contours and facilitating subsequent medical image analysis [14], [15]. Most current efficient segmentation models require a substantial amount of high-performance GPU computing resources for training and have a strong dependency on large-scale annotated data. However, obtaining high-quality annotated data requires a significant amount of time and human resources [16], [17].

Most current deep learning models for segmentation are based on UNet [18] and Transformer [19] architectures. UNet is renowned for its efficient and simple structure, which can effectively capture local features in images, while Transformers are known for their outstanding ability to capture global information [20]–[22]. The combination of UNet’s local feature extraction capabilities with the Transformer’s global information capture ability allows segmentation models to consider both local details and overall structure in images, thereby improving segmentation accuracy and robustness. This combination provides a more comprehensive and efficient solution for medical image analysis, offering strong support for advancements in the medical imaging field. However, the segmentation performance of most current methods is limited by the application scenario, and the robustness and generalization abilities of the models are usually weak. High-performance models like TransUNet [23], Swin-Unet [24], and MISSFormer [25] have demonstrated their capabilities primarily in segmenting eight organs in the heart and abdominal regions. UCTransNet [26] has expanded its tasks to include the segmentation of glands and cell nuclei. Nevertheless, in

This work was supported in part by the National Key Research and Development Program of China under Grant 2021YFE0102100, in part by the National Natural Science Foundation of China under Grant62303014, Grant62172002 and Grant 62322301, in part by the University Synergy Innovation Program of Anhui Province under Grant GXXT-2021-039 and Grant GXXT-2022-035, in part by Anhui Provincial Natural Science Foundation under Grant 2108085QF267 and Grant 2308085QF225, and in part by the Education Department of Anhui Province under Grant 2022AH020010 and Grant 2023AH050061. (Corresponding author: Yansen Su)

Rui Hao, Dayu Tan, Yansen Su, and Chunhou Zheng are with the Key Laboratory of Intelligent Computing and Signal Processing, Ministry of Education, Anhui University, Hefei 230601, China. (e-mail: tandayu19@163.com)

our actual experiments, we found that the segmentation performance of these methods varies significantly when applied to datasets with different image characteristics.

Existing works primarily focus on segmenting certain organs-at-risk and lesions, but they cannot segment multiple regions of the entire body, highlighting the limited application scenarios and the relatively poor robustness and generalization capabilities of these models. To address this, we propose conducting experiments on datasets that cover multiple organs-at-risk and tumors across the entire body. To enhance the model's generalization ability for different image characteristics, we intend to capture image features from multiple angles using multi-scale and multi-resolution images, enabling the model to better adapt to current application scenarios. Finally, we design the FCB (Flexible Connection Backbone), which is targeted for multi-region segmentation, as one of the strong backbones. Additionally, we design a SEB (Sharp Extraction Backbone) to assist the FCB in better feature extraction. Cascading the two backbones can ensure high segmentation performance while designing the model to enhance its robustness and generalization ability. Our contributions are summarized as follows:

- **Novel Multi-scale Cascaded Large-Model:** We propose a novel Multi-scale Cascaded U-shaped Network for whole-body ROI segmentation. This network cascades two backbone networks, namely our designed FCB (Flexible Connection Backbone) and SEB (Sharp Extraction Backbone). The two backbones are used to handle images of different scales and resolutions, with feature fusion occurring in the four skip connections and the down-sampling bottom layers of the network.
- **Innovative Adaptive Loss Aggregation Strategy:** We introduce a novel adaptive loss aggregation strategy named Adaptive-MFA (Adaptive Multi-scale Feature-Mixing Loss Aggregation). By using this strategy, we can create new prediction maps by combining available prediction maps, thereby optimizing the model training as much as possible.
- **Extensive Validation for Robustness and Generalization:** To thoroughly validate the model's robustness and generalization capabilities, we selected ten datasets targeting organs-at-risk and tumors throughout the body for experiments. The segmented regions include the brain, thoracic cavity, abdomen, and lower limbs, with two of these datasets provided by our collaborating hospital.

II. RELATED WORK

In this section, we introduce commonly used architectures for medical image segmentation as well as cascade network architectures.

A. Medical Image Segmentation

Medical image segmentation refers to accurately separating different structures (such as organs, lesion regions, etc.) in medical images, which is a crucial task in medical image analysis and computer-aided diagnosis. To address this task, research on U-shaped networks based on encoder-decoder

structures has seen explosive growth. UNet innovatively introduced the encoder-decoder architecture, enabling the aggregation of features from different stages through skip connections. Subsequently, UNet++ [28] and UNet 3+ [29] improved the skip connection mechanism, further enhancing the effectiveness of feature aggregation.

In recent years, the application of Transformers in medical image segmentation has attracted widespread attention. Originally used in the field of natural language processing, Transformers have shown great potential in computer vision tasks due to their powerful modeling capabilities and flexibility. Compared to traditional convolutional neural networks (CNNs), Transformer architectures primarily rely on self-attention mechanisms, allowing them to capture long-range dependencies in images globally. ViT [30] is one of the first models to apply Transformers to image classification tasks, processing images by splitting them into fixed-size patches and treating these patches as sequences inputted to the Transformer for processing. The same concept has been introduced into medical image segmentation, such as the TransUNet model, which significantly improves segmentation performance by combining the local feature extraction capability of UNet with the global contextual modeling capability of Transformers. Swin Transformer is a hierarchical Transformer architecture that further enhances computational efficiency and feature extraction capability through a sliding window mechanism. Swin-Unet applies this architecture to medical image segmentation tasks and achieves excellent results. Recently, Rahman et al. proposed the Cascaded MERIT [31] model, which effectively improves the accuracy and stability of medical image segmentation through techniques such as multiscale hierarchical feature extraction and cascaded attention decoding.

B. Cascaded Networks for Medical Image Segmentation

In recent years, cascade networks have gained considerable attention in medical image segmentation. These networks concatenate multiple modules, each handling specific subtasks, gradually improving overall segmentation performance. Cascade networks can integrate feature information at different scales and decompose tasks into multiple stages for optimization, with each stage utilizing feature representations from the preceding stage [31]. Information propagation is achieved through mechanisms such as skip connections and attention mechanisms. In experimental validation, cascade networks have demonstrated effectiveness and superiority in medical image segmentation tasks, offering significant potential as diagnostic and therapeutic tools in clinical medicine.

Recently, the CASCADE model introduced a novel attention-based decoder that learns local (contextual) relationships between pixels, addressing the shortcomings of Transformer models in learning local relationships. G-CASCADE [32] refines multi-stage feature maps generated by a hierarchical Transformer encoder through graph convolutional blocks, contributing to improved accuracy and robustness of segmentation results through progressive refinement. The Cascaded MERIT [31] model improves generalization capability by introducing a multiscale self-attention mechanism. Traditional

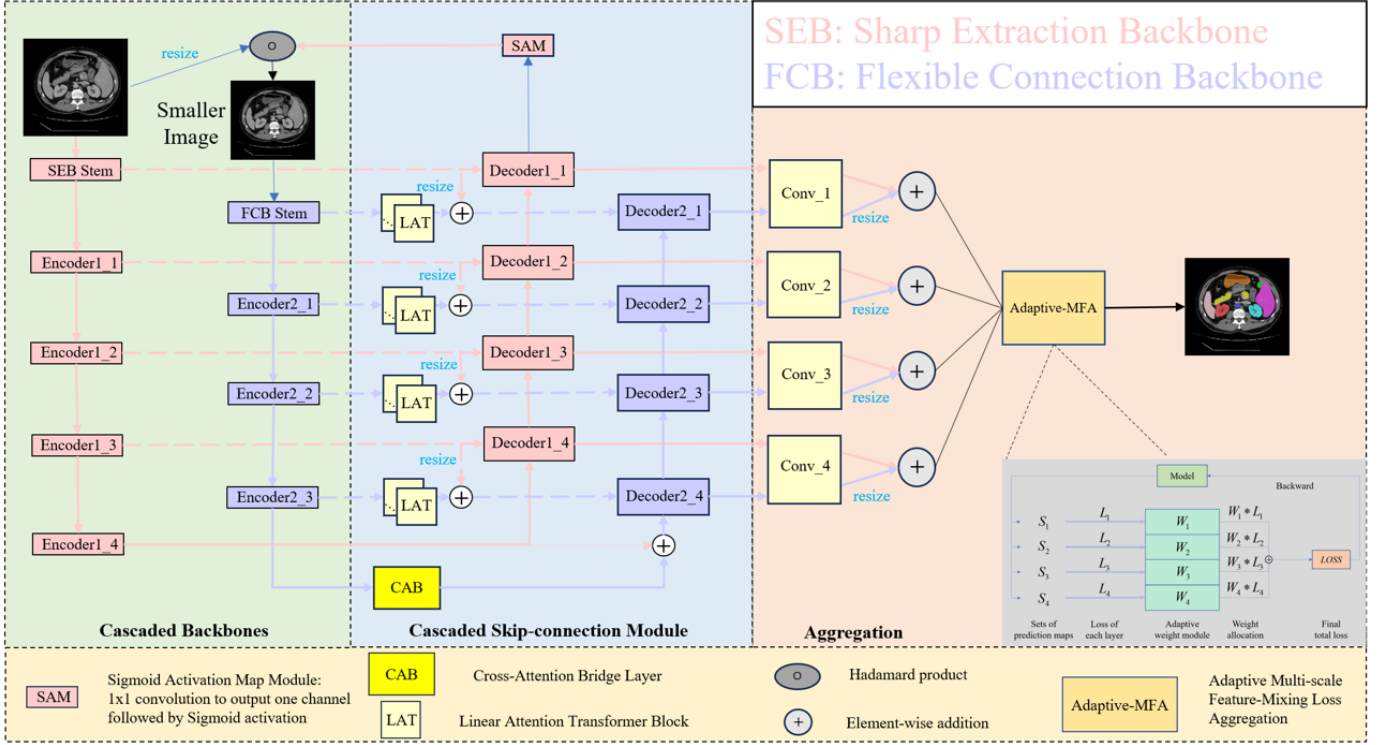


Fig. 1. Illustration of the overall architecture of MCFNet.

single-scale self-attention mechanisms may not effectively capture multiscale information in images, whereas Cascaded MERIT computes self-attention at multiple scales to comprehensively understand image features, thereby enhancing model performance. MCANet proposes a multi-scale cross-axis attention mechanism that efficiently captures information from different sizes and shapes of lesion regions or organs in medical images. By computing dual cross attentions between two parallel axial attentions, better global information capture is achieved, facilitating accurate segmentation of target areas in medical images.

III. PROPOSED METHOD

In this section, we introduce the multi-scale cascade network model MCFNet designed for whole-body ROI segmentation. First, we provide an overall introduction to the model, then we describe each component of the model in detail, and finally, we explain the adaptive loss aggregation strategy we designed.

A. MCFNet for Whole-body ROI Segmentation

Fig. 1 shows the overall architecture of our designed MCFNet network. MCFNet consists of three parts: Cascaded Backbones, Decoders with cascaded skip connections, and Aggregation. The Cascaded Backbones module is composed of SEB (Acute Extraction Backbone) and FCB (Elegant Connection Backbone), enabling multi-scale and multi-resolution input for the model. The Decoders with cascaded skip connections module mainly achieves feature aggregation at skip connections and bridge layers in the cascade network, enhancing feature representation by fully utilizing feature information

from different levels and different sub-networks. The Aggregation module primarily reflects the aggregation of the decoder output layers and the application of our designed adaptive loss aggregation strategy.

B. Cascaded Backbones in MCFNet

The cascaded backbone network consists of SEB (Sharp Extraction Backbone) and FCB (Flexible Connection Backbone). These two sub-backbone networks are responsible for feature extraction from images of different resolutions. Generally, high-resolution images can provide richer details and information, aiding the model in more accurately identifying and segmenting structures and regions within the images. However, this increases computational complexity and resource requirements. Low-resolution images are typically more robust to noise and interference but lose detailed information. Considering application requirements and computational resources, we choose to use FCB for processing 224×224 images and SEB for assisting with the processing of 256×256 images. In the encoder stage, the FCB sub-network uses traditional max pooling and convolution operations. This means that FCB has some limitations in feature extraction during the downsampling stage. Therefore, the design of SEB focuses on feature extraction during the downsampling stage while ensuring a relatively small number of parameters and computational load.

Specifically, SEB enhances the recognition and extraction of detailed features during the downsampling stage for high-resolution images by adding SE attention mechanisms to the encoding layers. As the feature extraction process deepens in SEB, the images go through BatchNorm, MaxPool, and

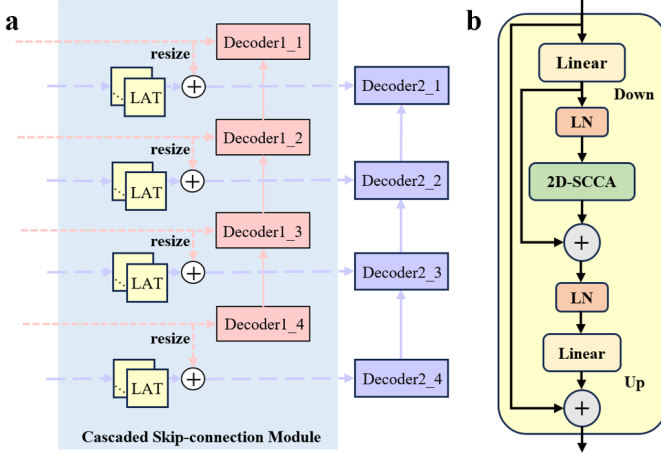


Fig. 2. (a) Illustration of the CSM (Cascaded Skip-connection Module). (b) Illustration of the LAT (Linear Attention Transformer Block) in the CSM.

convolution operations via the SEB Stem and encoding layers. The prediction map of SEB is finally output from the highest layer of the SEB decoder and is subjected to a Hadamard product operation with the input image of SEB to obtain a new output image. This new output image is then resized to the 224×224 input image required by FCB. The low-resolution images are input into FCB and processed through the FCB Stem and encoding layers. The four layers of feature maps are output through a skip connection mechanism and subsequently aggregated with those from SEB.

C. Cascaded Skip-connection Module in MCFNet

As shown in Fig. 2, this section mainly introduces the cascaded skip-connection mechanism. The efficient backbone model, FCB, is used to ensure the effectiveness of feature extraction, while a lightweight and simple SEB is employed to capture detailed information in high-resolution images, thus compensating for the limitations of FCB.

Specifically, when the encoding layers of FCB reach the lowest level after downsampling, they enter the CAB (Cross-Attention Bridge Layer). This module compensates for the loss of low-level features and then aggregates features with the output feature maps of the fourth encoding layer in SEB. For skip connections in FCB, the features first pass through the LAT (Linear Attention Transformer Block), enabling comprehensive and efficient feature extraction across both channel and spatial dimensions. As shown in Fig. 2, the structure of LAT is based on our published work, FSCA-Net, specifically the PAT (Parallel Attention Transformer Block). We make new improvements to accelerate the convergence speed of the transformer-like structure and reduce the number of model parameters caused by its architecture. After the input tensor enters the LAT module, we first use a linear layer for dimensionality reduction to align the tensor dimensions with the channel numbers. The compressed dimensional feature maps are then processed sequentially through layers including LN, 2D-SCCA attention, and another LN layer. Finally, we

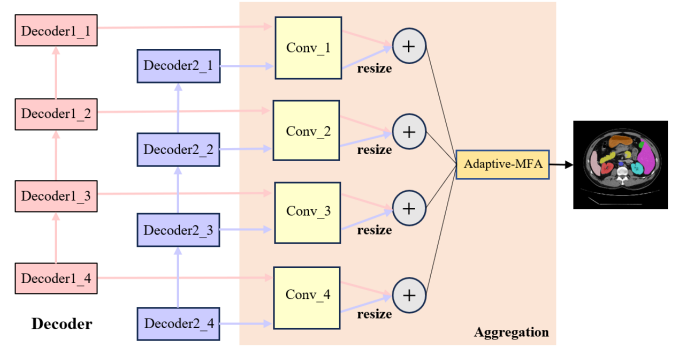


Fig. 3. Illustration of the Aggregation module.

obtain the output features by passing the data through a linear layer for dimensional restoration.

Subsequently, the feature maps outputted by LAT are aggregated with the feature maps outputted by the skip connections of resized SEB. The aggregated feature maps are then fed into the decoding layer of FCB through skip connections, which directly propagate shallow features to deeper layers, preserving fine-grained information captured by shallow networks. In SEB, the output prediction map (S_{output}) from the highest decoding layer is fed into the SAM (Sigmoid Activation Map Module). This module mainly utilizes a 1×1 convolution to output a single-channel feature map, and then applies the *Sigmoid* activation function to nonlinearly reweight features, enhancing the representation of key features while suppressing unimportant ones. The calculation formula for the SAM module is as follows:

$$Y(i, j) = w \cdot X(i, j) + b, \quad (1)$$

$$Z(i, j) = \sigma(Y(i, j)) = \frac{1}{1 + e^{-Y(i, j)}}, \quad (2)$$

where the weight is denoted as W , the input image is X (with dimensions $H \times W$), the output of the convolution operation is Y (with dimensions $H \times W$), the bias term is denoted as b , the output of the Sigmoid activation function is Z (with dimensions $H \times W$), and the values of the output image Z are constrained between 0 and 1. After the S_{output} undergoes the SAM operation, the final output image Z is obtained. This output image is then subjected to Hadamard product operation with the input image S_{input} of SEB, followed by a resize operation, as shown in the following formula:

$$\hat{O} = S_{input}(i, j) \cdot Z(i, j), \quad (3)$$

where \hat{O} is the output image obtained from the Hadamard product. The resize operation is implemented using bilinear interpolation. The bilinear interpolation is defined as follows:

$$\begin{aligned} f(x, y) = & (1 - \alpha) \cdot (1 - \beta) \cdot pixel(i_1, j_1) \\ & + \alpha \cdot (1 - \beta) \cdot pixel(i_2, j_2) \\ & + (1 - \alpha) \cdot \beta \cdot pixel(i_3, j_3) \\ & + \alpha \cdot \beta \cdot pixel(i_4, j_4), \end{aligned} \quad (4)$$

where the target image coordinates are denoted as (x, y) , the original image coordinates are (i, j) , and the four nearest

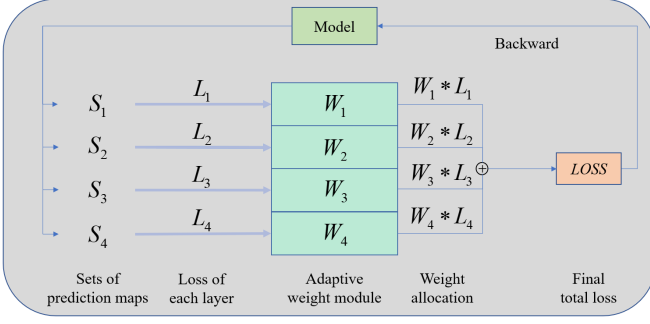


Fig. 4. Flowchart of the Adaptive-MFA Strategy.

neighbor pixels in the original image are $(i_1, j_1), (i_2, j_2), (i_3, j_3), (i_4, j_4)$. Additionally, $\alpha = x - i_1$, $\beta = y - j_1$, and $pixel(i, j)$ represent the pixel value at coordinates (i, j) in the original image. Each decoding layer of SEB and FCB generates a prediction map, representing the predicted results for the input. These prediction maps come from different scales and levels, reflecting different levels of feature information and semantic understanding. We feed these prediction maps into the Aggregation module for the aggregation of multi-scale information, aiming to comprehensively utilize information from different scales and improve the accuracy and robustness of the final prediction results.

D. Aggregation in MCFNet

As shown in Fig. 3, the module mainly summarizes the process of multi-scale feature aggregation in the decoding layer stage of two sub-networks, as well as the application of our newly designed adaptive loss aggregation strategy. Multi-scale feature aggregation helps the model utilize both global contextual information and local details, assisting the model in capturing finer image details and complex edge structures. This is particularly important for handling complex small structures in medical images, such as blood vessels and tumor boundaries. Moreover, merging features of different scales helps generate richer and more diverse feature representations, enabling the model to capture more comprehensive image information, effectively dealing with noise and deformation in images, and enhancing the segmentation capability for objects of different sizes. This allows the model to perform more stably across different types of medical images.

Specifically, the predicted maps output from the four layers of the encoding stage of SEB and B are pairwise fed into the corresponding convolutional blocks for channel-wise processing, obtaining feature maps with the desired specified number of channels. The calculation formula for this part is shown below:

$$O_i = Conv_{(C_i, N, K)}(E_i) (i = 1, 2, 3, 4), \quad (5)$$

where E refers to the input feature map, O refers to the output feature map, C is the number of input channels, N is the number of label classes, and K is the convolution kernel size. Additionally, $C_1 = 64, C_2 = 64, C_3 = 128, C_4 = 256$. After the convolution block operations, the two sub-networks use bilinear interpolation resizing to match the dimensions of the

output feature maps from FCB and SEB, followed by feature map aggregation. Subsequently, the four layers of different scale feature maps are fed into our designed adaptive loss aggregation strategy for prediction map data augmentation, thereby optimizing the training of the entire model. Through the adaptive search optimization accompanying the entire training process, the four layers of feature maps are aggregated to obtain the final output prediction map $Pred$ of the MCFNet model. The aggregation of the four layers of feature maps can be expressed by the following mathematical formula:

$$Pred = u \times p_1 + v \times p_2 + w \times p_3 + x \times p_4, \quad (6)$$

where p_1, p_2, p_3, p_4 represent the feature maps from the four prediction heads, and u, v, w, x are the corresponding weight coefficients for the four feature maps. In our experiments, we set all the weight coefficients to 1. In the following section, we will provide a detailed introduction to the adaptive loss aggregation strategy.

E. Adaptive-MFA: Adaptive Multi-scale Feature-Mixing Loss Aggregation

To better optimize model training, we have designed an adaptive loss aggregation strategy. The main idea is to create new prediction maps by combining available prediction maps. By integrating various prediction maps, the model can better handle errors in different situations. Adaptively selecting and weighting different prediction maps can optimize the final prediction results based on performance in different scenarios. This allows the model to better capture complex patterns in the data, thereby improving prediction accuracy.

The entire strategy flowchart is illustrated in the Fig. 4. Specifically, we randomly combine the output prediction maps P_1, P_2, P_3 and P_4 from the four layers of the decoder stage, resulting in a total of 15 non-empty subset combinations. Subsequently, we divide the 15 combinations into four sets S_1, S_2, S_3 and S_4 , and assign corresponding weights W_1, W_2, W_3 and W_4 to these sets. These weight coefficients are adaptively adjusted during model training. Regarding the setting of weight coefficients, since $W_1 + W_2 + W_3 + W_4 = 1$ imposes a competitive relationship among the four weight coefficients, it restricts the optimization of model training as it cannot account for all prediction map combinations. In other words, some prediction maps might contribute minimally to the optimization of the training loss but are still crucial for the model training process. Therefore, we discard the $W_1 + W_2 + W_3 + W_4 = 1$ restriction and only stipulate that the initial values satisfy $W_1 = W_2 = W_3 = W_4$. The specific contents of the four sets are as follows:

$$S_1 = \{ \{p_1\}, \{p_2\}, \{p_3\}, \{p_4\} \}, \quad (7)$$

$$S_2 = \{ \{p_1, p_2\}, \{p_1, p_3\}, \{p_1, p_4\}, \{p_2, p_3\}, \{p_2, p_4\}, \{p_3, p_4\} \}, \quad (8)$$

$$S_3 = \{ \{p_1, p_2, p_3\}, \{p_1, p_2, p_4\}, \{p_1, p_3, p_4\}, \{p_2, p_3, p_4\} \}, \quad (9)$$

$$S_4 = \left\{ \{p_1, p_2, p_3, p_4\} \right\}. \quad (10)$$

We perform feature map aggregation operations according to the combinations of each subset within each set. Subsequently, we calculate the total loss for each of the four sets, denoted as L_1 , L_2 , L_3 and L_4 . By incorporating the corresponding weight coefficients, we obtain the final total loss, $LOSS$, which is expressed as:

$$LOSS = W_1 * L_1 + W_2 * L_2 + W_3 * L_3 + W_4 * L_4, \quad (11)$$

the $LOSS$ obtained after each epoch during the training phase is fed back to the model itself, optimizing the model training and adaptively adjusting the weights. This process continues throughout the entire model training phase.

In summary, randomly combining and aggregating the outputs of the four-layer decoder allows full utilization of multi-level features, enhancing the model's predictive capability, robustness, and flexibility. This approach also provides new ideas and methods for model design and optimization. Furthermore, through experiments, we find that the weight coefficients of prediction maps tend to favor different sets across different datasets. Therefore, adaptively searching for the optimal weight coefficients better meets the demands of different scenarios, thereby improving the model's generalization ability and prediction accuracy. This adaptive search method dynamically adjusts weight distribution based on the characteristics of different datasets, enabling excellent performance across various scenarios.

IV. EXPERIMENTS

This section first introduces all 10 datasets used in the experiment, along with the quantitative and qualitative analyses of the experiment. Subsequently, we provide a detailed description of the parameter configurations used in the experiment. Finally, we outline the ablation study conducted for our proposed method.

A. Datasets

To validate the efficient segmentation of whole-body risk organs and lesions by MCFNet, we conduct experiments on ten datasets. The detailed descriptions of each dataset are as follows:

1) **HaN (2015)**: This is a public dataset for risk organs in the head and neck region, containing CT and MRI images of patients' head and neck. These patients underwent CT scans and T1-weighted MR imaging to support image-guided radiotherapy planning. The segmentation labels provided by the dataset are stored separately; we preprocessed the segmentation labels of six regions, merging them into one segmentation label file and classifying them in the order of brainstem, mandible, left parotid gland, right parotid gland, left submandibular gland, and right submandibular gland. After preprocessing the dataset, we divide the image data of 17 tumor patients into 14 cases for the training set and 3 cases for the test set, with the training set containing 1924 slices.

2) **SegTHOR (2019)**: This dataset is a CT dataset specifically for the segmentation of thoracic risk organs (OARs) and was included in the ISBI 2019 challenge. In this dataset, the risk organs for the segmentation task include the heart, trachea, aorta, and esophagus, which differ in spatial and appearance characteristics. After preprocessing the dataset, we divide the image data of 40 cases into 32 cases for the training set and 8 cases for the test set, with the training set containing 6035 slices.

3) **CHAOS (2019)**: As a multi-modal abdominal medical image segmentation dataset, it provides paired multi-modal CT and MRI data along with corresponding annotation information. MRI imaging data is obtained from two different sequences (T1-DUAL and T2-SPIR). Since the CT images only provide liver annotations, and the MRI images provide annotations for four organs (liver, spleen, left kidney, and right kidney), we select MRI imaging of 20 patients with two modalities. After preprocessing the dataset, we divide the image data of 40 cases into 32 cases for the training set and 8 cases for the test set, with the training set containing 1026 slices.

4) **LiTS (2017)**: This dataset focuses on the segmentation of the liver and its tumors in CT images. The data were collected from seven different medical centers and were included in the ISBI 2017, MICCAI 2017, and MICCAI 2018 segmentation challenges. From the original dataset of 131 patients, we randomly select data from 40 patients. After preprocessing the images, we obtain 32 cases for the training set and 8 cases for the test set, with the training set containing 4599 slices.

5) **KiTS (2019)**: This dataset is a CT dataset for the segmentation of kidneys and their tumors. It was included in the MICCAI 2019 challenge, which aimed to accelerate the development of reliable semantic segmentation methods for kidneys and kidney tumors. All data were sourced from arterial phase abdominal CT scans of 300 kidney cancer patients who underwent partial or radical nephrectomy, with ground truth labels for kidneys and tumors provided. From the 210 publicly available cases, we randomly select data from 80 patients. After preprocessing the images, we obtain 64 cases for the training set and 16 cases for the test set, with the training set containing 4754 slices.

6) **KiTS (2023)**: This dataset focuses on the segmentation of kidneys, tumors, and cysts, and is an extension of the KiTS (2019) dataset. It includes additional segmentation labels for cysts and increases the total data volume from 210 cases to 489 cases. This dataset was included in the MICCAI 2023 challenge. From the 489 patients' image data, we randomly select data from 80 patients for model validation. After preprocessing the data, we divide it into 64 cases for the training set and 16 cases for the test set, with the training set containing 4968 slices.

7) **LUNG (2018)**: This dataset is a subtask of the MSD Medical Image Segmentation Decathlon Challenge, aiming to segment lung tumors from CT images, highlighting the challenge of segmenting small targets within a large context. The official dataset includes thin-slice CT scans from 63 non-small cell lung cancer patients. After preprocessing the images,

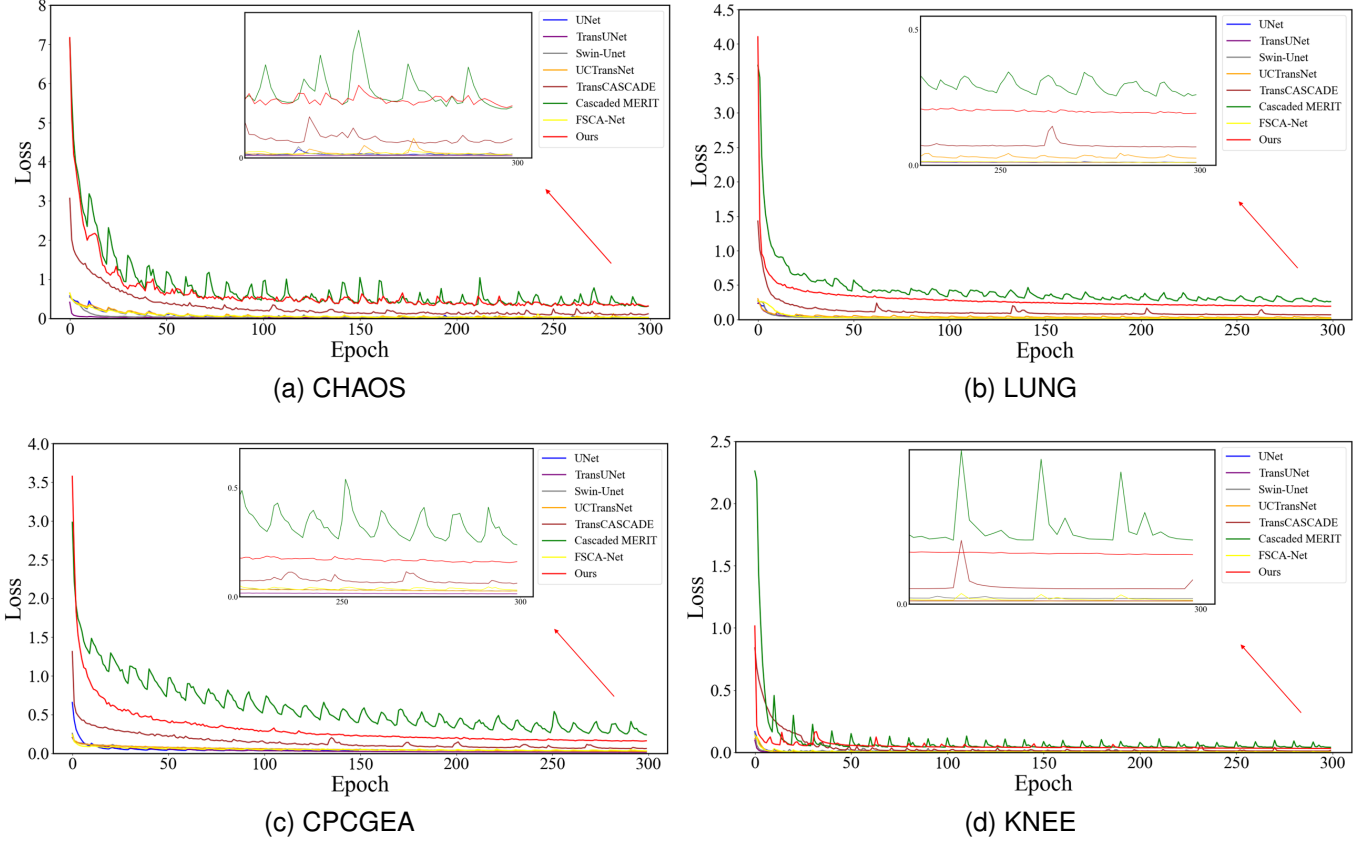


Fig. 5. Training loss trends of the proposed method and seven comparative methods across four datasets.

we divide the dataset into 50 cases for the training set and 13 cases for the test set, with the training set containing 1264 slices.

8) **CPCGEA (2023)**: This dataset includes MRI data of prostate cancer patients, comprising two modalities: DWI and T2WI sequences. The images suffer from poor clarity and additional noise due to environmental conditions or image sensor issues. Errors during image acquisition can also lead to artifacts such as streaks and shadows. The dataset consists of 172 cases with manually annotated prostate cancer regions. In our experiments, we randomly divide the data into 139 cases for the training set and 33 cases for the test set, with the training set containing 832 slices.

9) **KNEE (2023)**: This dataset consists of MRI images of patients' leg bones, focusing on the segmentation of the femur. It includes MRI image data from 59 patients. After preprocessing the images, we obtain 47 cases for the training set and 12 cases for the test set, with the training set containing 8171 slices.

10) **AutoPET (2023)**: AutoPET is a large-scale PET/CT dataset focusing on whole-body tumor segmentation, included in the MICCAI 2022 and MICCAI 2023 challenges. The official dataset comprises 1014 paired PET-CT images from 900 patients. Each data instance includes a three-dimensional whole-body FDG-PET image, a three-dimensional whole-body CT image, and a manually annotated three-dimensional tumor mask. Notably, all CT and PET images were acquired in

the same scanning session using the same PET/CT scanner, ensuring high anatomical consistency. The dataset primarily covers patients with histologically confirmed malignant melanoma, lymphoma, and lung cancer, as well as negative control patients who underwent FDG-PET/CT scans at the University Hospital of Tübingen and LMU University Hospital in Munich, Germany. In our experiments, we select the PET images and annotations. We randomly divide the data from 80 patients into 64 cases for the training set and 16 cases for the test set, with the training set containing 2558 slices.

B. Evaluation Metrics

In all experiments, we comprehensively evaluate the performance of the segmentation models by applying appropriate metrics based on the dataset type.

For segmentation tasks on multi-class datasets, we use two key evaluation metrics: the Dice Similarity Coefficient (DSC) and the 95% Hausdorff Distance (HD95). DSC measures the overlap between the predicted segmentation and the ground truth, with higher values indicating better segmentation performance. HD95 assesses the boundary deviations in the segmentation results, where smaller values reflect higher accuracy in boundary prediction.

For segmentation tasks on single-class datasets, we use four evaluation metrics: DSC, HD95, Recall, and Precision. In addition to DSC and HD95, Recall measures the model's ability to detect all instances of the target class, showing how

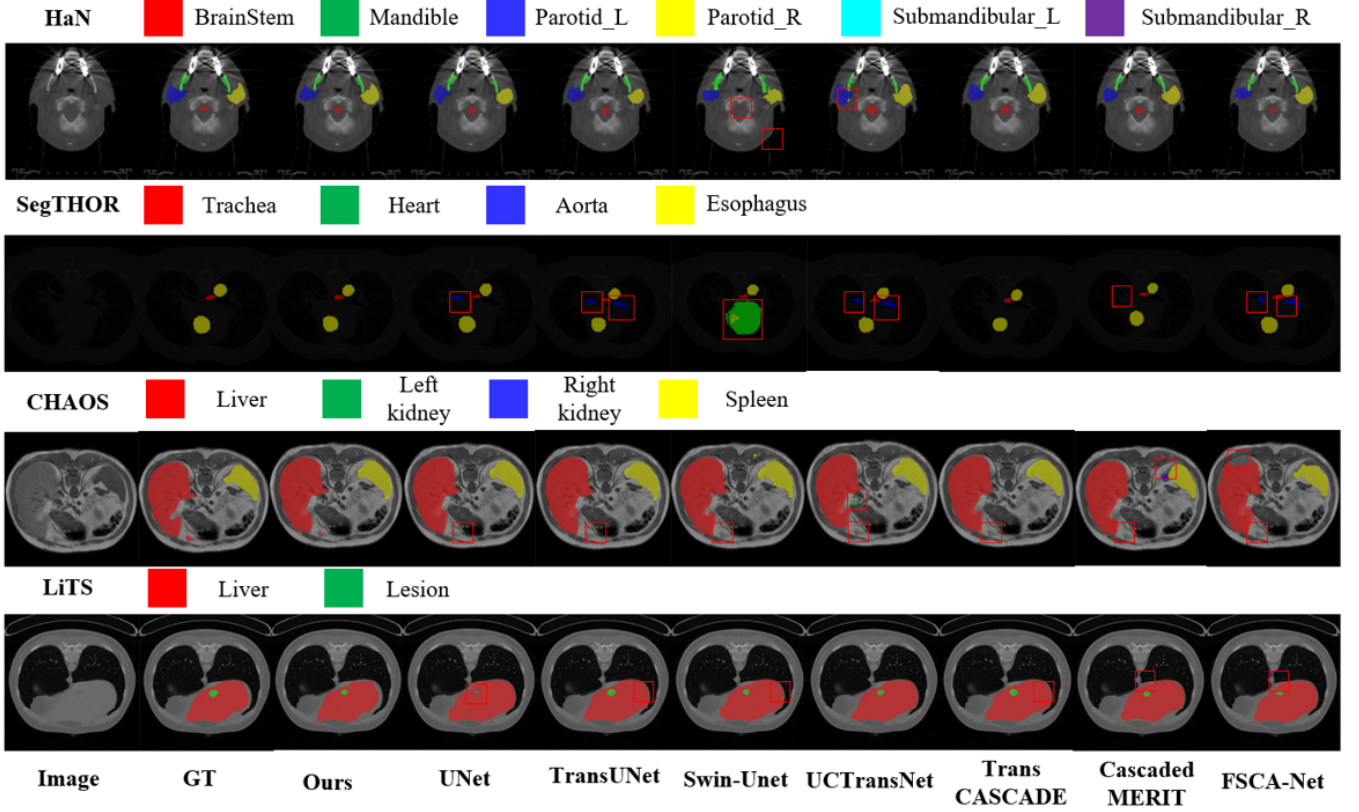


Fig. 6. Visual examples of segmentation on the HaN, SegTHOR, CHAOS, and LiTS datasets.

well the model captures the entire target region. Precision measures the proportion of correctly identified target regions among all predicted positives, evaluating the model's ability to avoid false positives. By combining these four metrics, we can more comprehensively and accurately assess the performance of single-class segmentation models.

C. Implementation Detail

All experiments are conducted on a NVIDIA A6000 GPU. We standardize the resolution of all input images to 256×256 . The max training epoch is 300 with a batch size of 16 for all experiments. We use the Adam optimizer for model training with an initial learning rate of 0.001 and a cosine annealing learning rate decay strategy. The weight decay is set to 0.0001. The loss function used is a combination of Dice Loss and Cross-Entropy Loss. It can be defined as:

$$L(Y, P) = 1 - \sum_{i=1}^I \left(\lambda \frac{2 * \sum_{n=1}^N Y_{n,i} \cdot P_{n,i}}{\sum_{n=1}^N Y_{n,i}^2 + \sum_{n=1}^N P_{n,i}^2} + \sum_{n=1}^N Y_{n,i} \log P_{n,i} \right), \quad (12)$$

I is the number of classes, N is the total number of voxel. $Y_{n,i}$ and $P_{n,i}$ are the ground truth and output probability for the i -th class at voxel n , respectively.

D. Comparison With Other Methods

We employ seven state-of-the-art methods to validate the performance of MCFNet: U-Net, TransUNet, Swin-Unet, UC-TransNet, TransCASCADE, Cascaded MERIT, and FSCA-Net. We validate the segmentation performance of our proposed method against seven comparison models across all ten datasets. In Fig. 5, the training loss trends of all methods are illustrated across the four datasets. Fig. 5 shows visual examples of segmentation on all datasets and we highlight incorrectly segmented areas with red boxes. The specific qualitative and quantitative analysis results are as follows:

1) *Experiments on HaN*: Our proposed method and seven comparison models segment six regions in this dataset. As shown in the Table I, the Cascaded MERIT model achieves excellent segmentation performance, with an average DSC of 74.71% and an average HD95 of 2.532mm. Our designed MCFNet improves the average DSC by 2.81% and reduces the average HD95 by 0.079mm compared to Cascaded MERIT. The experimental results in Table I show that our model significantly improves the segmentation of the left submandibular gland.

As shown in the first row of Fig. 6, we observe that our proposed method does not exhibit under-segmentation or over-segmentation compared to the comparison models. For example, UNet incorrectly identifies the mandibular region, while Swin-Unet fails to fully recognize the brainstem region, resulting in under-segmentation. Additionally, UCTransNet fails to accurately distinguish between the left and right parotid

TABLE I
COMPARISONS WITH STATE-OF-THE-ART MODELS ON THE HAN DATASET.

Method	DSC \uparrow (%, mean)	HD95 \downarrow (mm, mean)	BrainStem	Mandible	Parotid_L	Parotid_R DSC \uparrow (%)	Submandibular_L	Submandibular_R
UNet	72.98	3.260	77.44	89.45	73.68	76.09	59.08	62.17
TransUNet	71.48	5.412	76.12	90.81	71.97	71.16	56.96	61.82
Swin-Unet	68.75	7.541	73.51	91.67	70.53	73.27	50.63	52.85
UCTransNet	70.36	4.328	77.26	88.85	70.38	71.03	61.23	53.43
TransCASCADE	71.56	3.184	79.39	87.67	70.75	75.20	51.44	64.89
Cascaded MERIT	74.71	2.532	79.17	92.14	75.70	78.57	54.78	67.89
FSCA-Net	73.31	4.822	75.52	90.19	73.62	72.36	64.06	64.11
Ours	77.52	2.453	79.52	93.47	77.59	78.61	68.02	67.92

TABLE II
COMPARISONS WITH STATE-OF-THE-ART MODELS ON THE SEGTHOR DATASET.

Method	DSC \uparrow (%, mean)	HD95 \downarrow (mm, mean)	Trachea	Heart	Aorta DSC \uparrow (%)	Esophagus
UNet	75.30	6.190	56.06	84.27	82.25	78.62
TransUNet	80.79	4.542	64.24	88.31	84.70	85.91
Swin-Unet	71.32	7.208	47.12	85.60	77.43	75.15
UCTransNet	80.86	5.115	64.36	87.91	85.32	85.85
TransCASCADE	77.18	4.608	58.54	89.26	80.37	80.55
Cascaded MERIT	78.92	4.272	59.16	89.30	83.65	83.58
FSCA-Net	80.75	4.947	65.56	85.84	84.48	87.12
Ours	83.27	4.187	69.37	89.55	87.75	87.40

TABLE III
COMPARISONS WITH STATE-OF-THE-ART MODELS ON THE CHAOS DATASET.

Method	DSC \uparrow (%, mean)	HD95 \downarrow (mm, mean)	Liver	Kidney_L	Kidney_R DSC \uparrow (%)	Spleen
UNet	90.82	8.990	94.02	90.42	90.43	88.43
TransUNet	91.19	5.902	94.40	91.92	91.06	87.40
Swin-Unet	90.17	4.366	93.61	90.23	89.65	87.20
UCTransNet	88.94	6.522	91.26	90.05	86.96	87.49
TransCASCADE	90.26	3.695	93.66	91.61	89.79	85.99
Cascaded MERIT	90.69	3.914	93.57	91.25	91.74	86.18
FSCA-Net	89.83	9.277	93.55	91.12	88.25	86.41
Ours	92.80	3.676	94.87	93.45	92.05	90.83

glands.

2) *Experiments on SegTHOR*: Our proposed method and seven comparison models segment the trachea, heart, aorta, and esophagus in this dataset. According to the experimental results in Table II, current state-of-the-art methods such as TransUNet, UCTransNet, and FSCA-Net achieve over 80% in average DSC and reduce the average HD95 to below 5mm. Our proposed method achieves an average DSC of 83.27% and an average HD95 of 4.187mm, with MCFNet obtaining the best performance in segmenting the trachea, heart, aorta, and esophagus.

As shown in the second row of Fig. 6, our designed model accurately identifies and segments the risk organs. However, UNet, TransUNet, UCTransNet, Cascaded MERIT, and FSCA-Net all mistakenly identify the background as the aorta. Additionally, Swin-Unet incorrectly identifies the esophagus region as the heart.

3) *Experiments on CHAOS*: The comparison results are shown in Table III. We can see that the cascade networks TransCASCADE [33] and Cascaded MERIT achieve relatively good segmentation results for the four abdominal organs, with average DSCs of 90.26% and 90.69%, and average HD95s of 3.695mm and 3.914mm, respectively. The traditional TransUNet achieves an average DSC of 91.19%, making it the

TABLE IV
COMPARISONS WITH STATE-OF-THE-ART MODELS ON THE LITS DATASET.

Method	DSC \uparrow (%, mean)	HD95 \downarrow (mm, mean)	Liver	Lesion DSC \uparrow (%)
UNet	64.10	31.754	92.11	36.11
TransUNet	71.46	25.951	90.97	51.93
Swin-Unet	66.09	30.759	91.83	40.35
UCTransNet	66.77	29.473	92.66	40.87
TransCASCADE	72.56	25.351	94.16	50.96
Cascaded MERIT	72.36	24.521	93.25	51.47
FSCA-Net	68.54	23.897	93.04	44.04
Ours	73.79	23.326	94.22	53.35

TABLE V
COMPARISONS WITH STATE-OF-THE-ART MODELS ON THE KITS (2019) DATASET.

Method	DSC \uparrow (%, mean)	HD95 \downarrow (mm, mean)	Kidney	Lesion DSC \uparrow (%)
UNet	65.20	23.039	87.99	42.41
TransUNet	66.41	34.096	89.52	43.31
Swin-Unet	65.21	33.455	85.09	45.33
UCTransNet	64.31	43.377	87.25	41.37
TransCASCADE	68.14	25.023	89.78	46.43
Cascaded MERIT	68.50	22.970	90.29	46.38
FSCA-Net	60.59	41.617	85.97	35.22
Ours	70.71	20.522	90.50	50.92

best-performing model among the comparisons. Our designed model achieves an average DSC of 92.80% and reduces the average HD95 to 3.676mm, significantly outperforming all comparison models.

As shown in the third row of Fig. 6, most comparison models exhibit under-segmentation for the liver region, and Cascaded MERIT also shows ambiguous identification for the spleen and right kidney. Our designed model generally achieves accurate segmentation, but there is still room for improvement in the segmentation of the spleen's edges.

4) *Experiments on LiTS*: All results for this dataset are shown in Table IV. We can see that TransCASCADE is the best-performing advanced segmentation method, achieving an average DSC of 72.56%. For liver tumor segmentation, TransUNet achieves a DSC of 51.93%, which is currently the best. Our designed model achieves better segmentation results for tumors, with an average DSC of 73.79% and a DSC of 53.35% for tumor regions.

As shown in the fourth row of Fig. 6, our designed model, like many comparison models, achieves relatively accurate

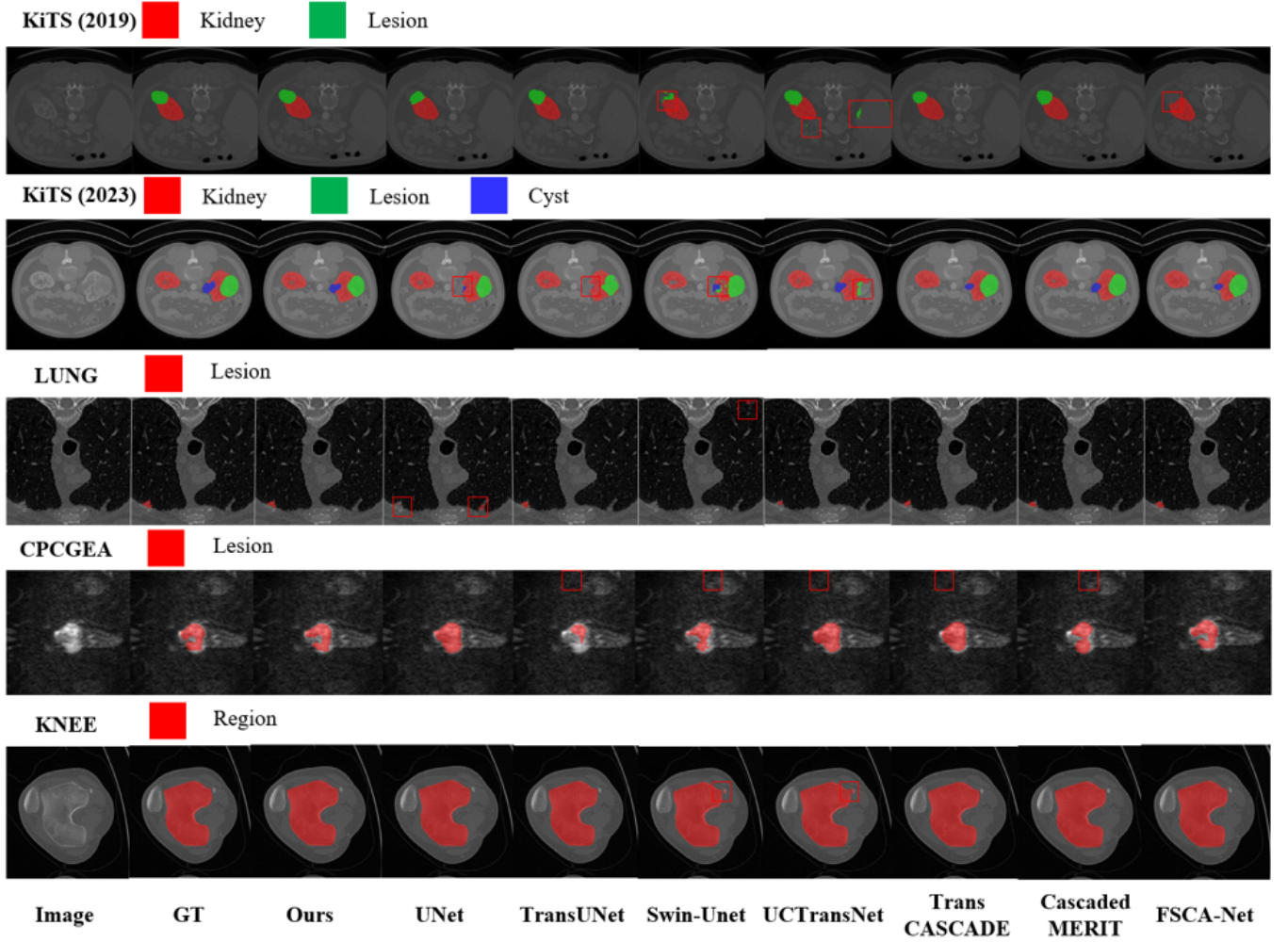


Fig. 7. Visual examples of segmentation on the KiTS (2019), KiTS (2023), LUNG, CPCGEA and KNEE datasets.

TABLE VI
COMPARISONS WITH STATE-OF-THE-ART
MODELS ON THE KITS (2023) DATASET.

Method	DSC \uparrow (%, mean)	HD95 \downarrow (mm, mean)	Kidney	Lesion DSC \uparrow (%)	Cyst
UNet	51.79	30.987	90.14	33.02	32.20
TransUNet	58.31	29.390	90.94	42.31	41.68
Swin-Unet	49.41	31.283	87.02	35.52	25.69
UCTransNet	47.19	44.911	87.92	18.86	34.79
TransCASCADE	59.38	26.173	91.21	44.76	42.17
Cascaded MERIT	61.01	23.033	91.29	45.05	46.69
FSCA-Net	46.55	28.441	90.67	21.83	27.16
Ours	64.07	22.770	91.74	45.18	55.31

TABLE VII
COMPARISONS WITH STATE-OF-THE-ART
MODELS ON THE LUNG DATASET.

Method	DSC \uparrow (%, mean)	HD95 \downarrow (mm, mean)	Recall \uparrow (%, mean)	Precision \uparrow (%, mean)
U-Net	70.50	37.913	66.07	80.04
TransUNet	70.72	25.218	60.56	82.06
SwinUnet	63.41	25.131	57.47	77.29
UCTransNet	70.75	32.384	65.90	80.38
TransCASCADE	68.31	28.551	65.01	76.51
Cascaded MERIT	70.43	28.554	67.33	83.34
FSCA-Net	72.10	25.545	68.07	82.23
Ours	74.49	23.505	71.06	83.52

segmentation for the liver and liver tumors. However, there is a gap in the detailed segmentation of the tumor region edges. Additionally, models like UNet, due to the small size of the segmentation target, may fail to recognize the tumor region.

5) *Experiments on KiTS (2019)*: This dataset focuses on the segmentation of kidneys and kidney tumors. As shown in Table V, our designed model achieves an average DSC that is 2.21% higher than the state-of-the-art model Cascaded MERIT and an average HD95 that is 2.448mm lower. Additionally, MCFNet improves the tumor segmentation DSC by 4.49% compared to

TransCASCADE.

As shown in the fifth row of Fig. 7, we demonstrate the segmentation effects of the models on an image containing both the kidney and tumor. Swin-Unet exhibits scattered segmentation in the tumor region, with dispersed pixels. UCTransNet mistakenly identifies some background areas as tumors. Even more problematic, FSCA-Net fails to recognize the tumor region altogether.

6) *Experiments on KiTS (2023)*: This dataset builds upon the segmentation labels of kidneys and kidney tumors from

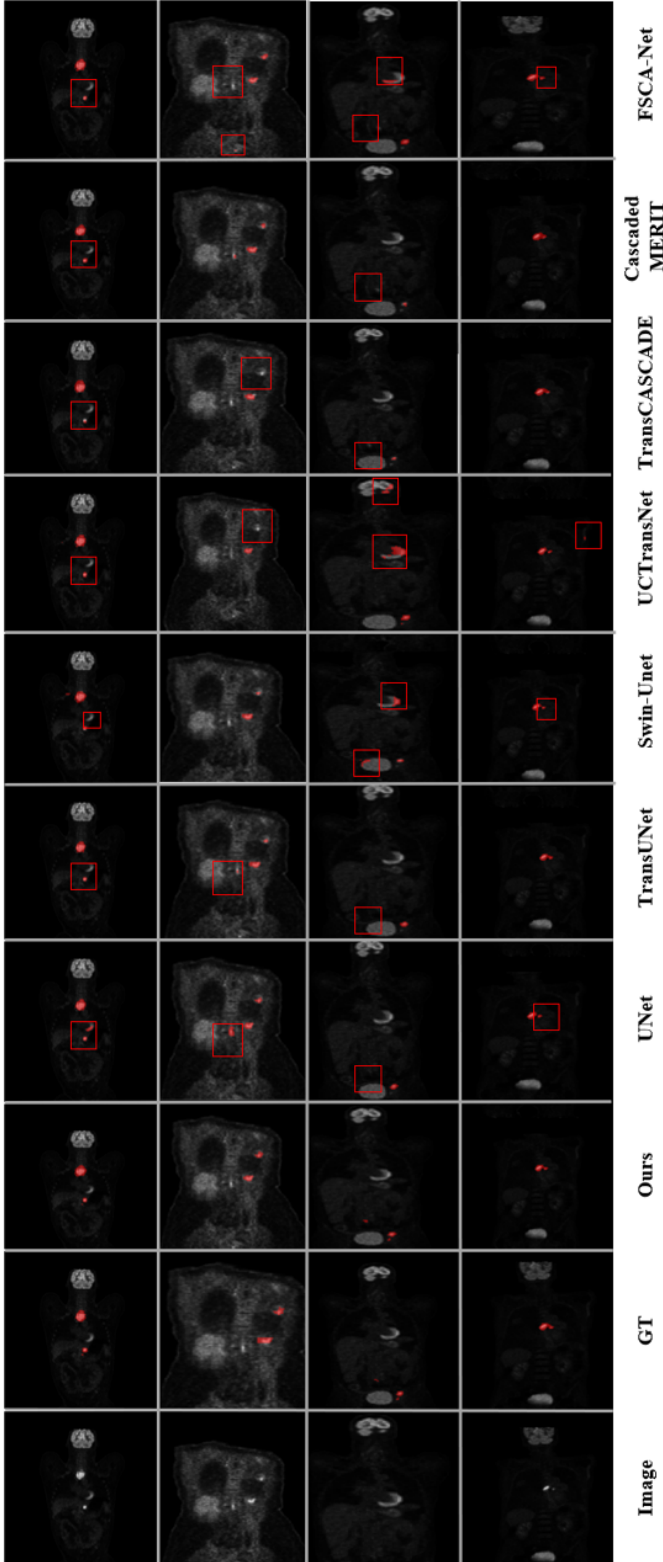


Fig. 8. Visual examples of segmentation on the AutoPET dataset.

KiTS (2019) by adding segmentation for cysts. As shown in Table VI, traditional networks do not perform well in the segmentation of tumors and cysts. For example, the best-performing TransUNet achieves an average DSC of only

TABLE VIII
COMPARISONS WITH STATE-OF-THE-ART
MODELS ON THE CPCGEA DATASET.

Method	DSC \uparrow (%, mean)	HD95 \downarrow (mm, mean)	Recall \uparrow (%, mean)	Precision \uparrow (%, mean)
U-Net	64.05	9.312	70.34	65.99
TransUNet	63.18	8.517	70.02	66.14
SwinUnet	60.94	7.185	66.20	65.24
UTransNet	60.25	11.374	67.59	64.78
TransCASCADE	65.44	6.646	68.85	69.14
Cascaded MERIT	65.50	7.738	70.47	68.57
FSCA-Net	65.24	6.792	68.88	68.37
Ours	67.28	6.064	71.48	69.43

TABLE IX
COMPARISONS WITH STATE-OF-THE-ART
MODELS ON THE KNEE DATASET.

Method	DSC \uparrow (%, mean)	HD95 \downarrow (mm, mean)	Recall \uparrow (%, mean)	Precision \uparrow (%, mean)
U-Net	98.99	1.089	98.65	99.23
TransUNet	98.92	1.094	98.74	99.12
SwinUnet	98.25	1.228	97.79	98.72
UTransNet	99.08	1.055	98.82	99.01
TransCASCADE	99.02	1.000	98.89	99.16
Cascaded MERIT	99.09	1.000	98.95	99.24
FSCA-Net	97.59	5.362	97.00	98.43
Ours	99.14	1.000	98.99	99.29

TABLE X
COMPARISONS WITH STATE-OF-THE-ART
MODELS ON THE AUTOPET DATASET.

Method	DSC \uparrow (%, mean)	HD95 \downarrow (mm, mean)	Recall \uparrow (%, mean)	Precision \uparrow (%, mean)
U-Net	58.49	30.832	59.82	68.62
TransUNet	61.95	22.329	60.22	72.98
SwinUnet	50.55	31.925	53.67	57.58
UTransNet	58.05	28.279	59.77	65.51
TransCASCADE	55.18	24.160	49.92	73.31
Cascaded MERIT	58.32	23.407	57.10	69.09
FSCA-Net	61.53	26.707	62.07	70.76
Ours	63.87	22.251	65.35	73.91

42.31% for tumors and 42.68% for cysts. In contrast, our designed model improves the DSC for cyst segmentation to 55.31%, and MCFNet achieves the best performance in segmentation for kidneys, kidney tumors, and cysts.

As shown in the sixth row of Fig. 7, the addition of cyst segmentation labels increases the difficulty of segmenting small target areas. Models like UNet, TransUNet, and Swin-Unet demonstrate shortcomings in segmenting cysts effectively. Additionally, while UTransNet accurately identifies cyst regions, it struggles to maintain accurate recognition of tumor regions simultaneously.

7) *Experiments on LUNG*: In this dataset, we select four evaluation metrics to validate the model's segmentation performance, as shown in Table VII. It is observed that the advanced model FSCA-Net achieves the best results in terms of DSC and Recall, while Cascaded MERIT achieves the best Precision among existing models, reaching 82.23%. Our designed model achieves the best performance across DSC, HD95, Recall, and Precision metrics. Specifically, MCFNet improves DSC by a significant 2.39% and Recall by 2.99% compared to FSCA-

TABLE XI
ABLATION EXPERIMENTS ON FIVE DATASETS.

Method	SegTHOR		CHAOS		LITS		KiTS19		CPCGEA			
	DSC \uparrow (%, mean)	HD95 \downarrow (mm, mean)	DSC \uparrow (%, mean)	HD95 \downarrow (mm, mean)	DSC \uparrow (%, mean)	HD95 \downarrow (mm, mean)	DSC \uparrow (%, mean)	HD95 \downarrow (mm, mean)	DSC \uparrow (%, mean)	HD95 \downarrow (mm, mean)	Recall \uparrow (%, mean)	Precision \uparrow (%, mean)
SEB	78.74	5.063	90.17	6.051	66.47	26.199	67.32	33.096	63.18	8.520	70.02	66.14
FCB	80.75	4.947	89.83	9.277	68.54	23.897	60.59	41.617	65.24	6.792	68.88	68.37
SEB+Adaptive-MFA	79.72	5.220	90.44	4.366	67.75	35.554	67.84	30.069	63.75	7.746	75.76	59.78
SCB+Adaptive-MFA	81.43	5.040	90.01	8.253	70.56	25.951	64.31	43.377	65.44	6.646	68.85	69.14
SEB+FCB	82.87	5.306	91.91	6.001	73.25	26.803	68.32	23.997	65.50	7.738	70.47	68.57
SEB+FCB+Adaptive-MFA	83.27	4.187	92.80	3.676	73.79	23.326	70.71	20.522	67.28	6.064	71.48	69.43

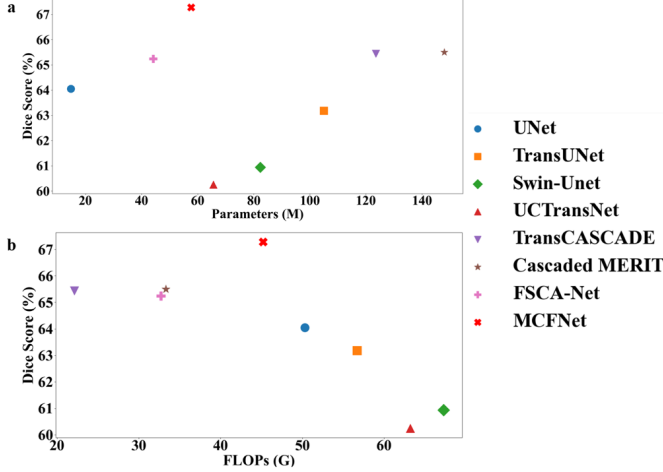


Fig. 9. The experiments shown in the figure are conducted on the CPCGEA dataset. (a) Visualization of model performance and parameter size. (b) Visualization of model performance and FLOPs.

Net.

As shown in the seventh row of Fig. 7, for single-label segmentation targets, most models correctly identify tumor regions except for Swin-Unet. UNet identifies tumor regions but also mistakenly includes background areas as tumors. Swin-Unet not only fails to accurately identify tumor regions but also misidentifies vascular regions in the background as tumors.

8) *Experiments on CPCGEA*: As shown in Table VIII, we compare seven comparison models for the segmentation performance of prostate cancer. Since we are dealing with single-label image segmentation, we use four evaluation metrics to comprehensively assess model performance. Our designed model improves upon the current best model by 1.78% in DSC, reduces HD95 by 0.582mm, increases Recall by 1.01%, and improves Precision by 0.29%.

As shown in the eighth row of Fig. 7, we continue the work initiated by our previously proposed model, FSCA-Net, and conducted further exploration on CPCGEA. We add experiments with TransCASCADe and Cascaded MERIT, revealing that they exhibit unclear boundary segmentation for prostate cancer regions and struggle to delineate the edges of tumor areas effectively.

9) *Experiments on KNEE*: As shown in Table IX, all models achieve an average DSC for femur segmentation exceeding 97.5%, with our designed model achieving the highest at 99.14%. Additionally, HD95, Recall, and Precision also

achieve optimal performance, although the improvement in segmentation performance compared to advanced models is relatively limited.

As depicted in the ninth row of Fig. 7, we can see that all models accurately segment the femur region. However, Swin-Unet and UCTransNet exhibit minor segmentation errors in very small areas, although the overall differences are minimal.

10) *Experiments on AutoPET*: For whole-body tumor segmentation, our designed model and seven comparison models are evaluated using four metrics, as shown in the Table X. Among the current advanced methods, TransUNet achieves the best DSC of 61.95%, the best HD95 of 22.329mm, and the best Precision of 72.98%. Additionally, FSCA-Net achieves a Recall of 62.07%. However, our designed model MCFNet improves by 1.92% in DSC, reduces HD95 by 0.078mm, increases Recall by 3.28%, and improves Precision by 0.93%.

As shown in Fig. 8, four segmentation cases from the AutoPET dataset are presented. The erroneous segmentation areas are all marked with red boxes. In the whole-body tumor segmentation images, there are many background areas that appear white and have smooth edges but are not tumors, leading the segmentation models to mistakenly identify tumor regions. From a comprehensive observation of the four cases, it can be seen that most models exhibit confusion between the background and tumor regions. Specifically, UNet and TransUNet have issues with over-segmentation and under-segmentation. Swin-Unet, UCTransNet, and FSCA-Net all display errors in segmentation, while TransCASCADe and Cascaded MERIT show cases of under-segmentation. Although the MCFNet model has performed relatively well in tumor segmentation, there is still room for improvement in segmenting the detailed boundaries of tumor regions.

E. Ablation Study

To validate the effectiveness of our proposed module, we conduct experiments on five datasets and use multiple evaluation metrics to comprehensively assess the module's effectiveness. As shown in Table XI, after applying the adaptive loss aggregation strategy to SEB and FCB, the segmentation performance significantly improves across all datasets. Additionally, compared to using SEB and FCB individually, cascading SEB and FCB enhances the model's segmentation performance, and further applying the adaptive loss aggregation strategy on top of this results in the best segmentation performance.

F. Discussion

MCFNet integrates low parameter count, low computational cost, and high segmentation performance. Our designed

model effectively balances performance with parameter and computational cost, demonstrating significant advantages over existing state-of-the-art methods. To illustrate this, we conduct experiments on the CPCGEA dataset and compare our model's results with several benchmark models. These experimental results are visualized in figures, clearly showing the performance of the MCFNet model. As shown in Fig. 9, our model not only exhibits excellent segmentation performance but also achieves or surpasses the performance of existing methods while maintaining a smaller parameter size and lower computational cost. This indicates that our model offers higher efficiency and better scalability in practical applications. The optimization of performance, computational cost, and parameter size makes our model suitable for resource-constrained environments and lays a solid foundation for its future promotion and application in various scenarios.

V. CONCLUSION

We design a novel multi-scale, multi-resolution cascade fusion network called MCFNet. By capturing rich image features from multi-scale and multi-resolution images, our designed model is better suited to various application scenarios. We propose an adaptive loss aggregation strategy called Adaptive-MFA to optimize model training and performance. We conduct experiments on multiple datasets covering whole-body risk organs and tumors to fully validate the robustness and generalization capability of the model. Experimental results show that our MCFNet exhibits excellent segmentation performance and good generalization ability across multiple datasets.

In practical clinical applications, the efficient segmentation capability of MCFNet can significantly enhance the accuracy and efficiency of medical image analysis, reduce the workload of doctors, and improve the precision of diagnosis and treatment. By accurately segmenting risk organs and tumor regions, MCFNet can assist doctors in better formulating treatment plans, thereby improving patient outcomes. Additionally, the good generalization ability of MCFNet means it can adapt to image data generated by different hospitals and equipment, making it a promising tool for widespread use in clinical practice. This can drive advancements and progress in the field of medical image analysis.

REFERENCES

- [1] J. Ma et al., "Segment anything in medical images," *Nat. Commun.*, vol. 15, p. 654, 2024.
- [2] A. He et al., "H2Former: An Efficient Hierarchical Hybrid Transformer for Medical Image Segmentation," *IEEE Trans. Med. Imaging*, vol. 42, no. 9, pp. 2763-2775, 2023.
- [3] R. Atun et al., "Expanding global access to radiotherapy," *Lancet Oncol.*, vol. 16, no. 10, pp. 1153-1186, 2015.
- [4] G. Delaney et al., "The role of radiotherapy in cancer treatment: Estimating optimal utilization from a review of evidence-based clinical guidelines," *Cancer*, vol. 104, pp. 1129-1137, 2005.
- [5] R. Baskar et al., "Cancer and radiation therapy: Current advances and future directions," *Int. J. Med. Sci.*, vol. 9, pp. 193-199, 2012.
- [6] F. Shi et al., "Deep learning empowered volume delineation of whole-body organs-at-risk for accelerated radiotherapy," *Nat. Commun.*, vol. 13, pp. 6566, 2022.
- [7] D. De Ruyscher et al., "Radiotherapy toxicity," *Nat. Rev. Dis. Prim.*, vol. 5, p. 13, 2019.
- [8] E. Huynh et al., "Artificial intelligence in radiation oncology," *Nat. Rev. Clin. Oncol.*, vol. 17, pp. 771-781, 2020.
- [9] C. R. Deig et al., "Artificial intelligence in radiation oncology," *Hematol. Oncol. Clin. North Am.*, vol. 33, pp. 1095-1104, 2019.
- [10] G. Wang et al., "Deepigeos: a deep interactive geodesic framework for medical image segmentation," *IEEE Trans. Pattern Anal. Mach. Intell.*, vol. 41, no. 7, pp. 1559-1572, 2018.
- [11] G. Wang et al., "Interactive medical image segmentation using deep learning with image-specific fine tuning," *IEEE Trans. Med. Imaging*, vol. 37, no. 7, pp. 1562-1573, 2018.
- [12] T. Zhou et al., "Volumetric memory network for interactive medical image segmentation," *Med. Image Anal.*, vol. 83, p. 102599, 2023.
- [13] C. Fang et al., "Reliable Mutual Distillation for Medical Image Segmentation Under Imperfect Annotations," *IEEE Trans. Med. Imaging*, vol. 42, no. 6, pp. 1720-1734, 2023.
- [14] D. Tan et al., "Multi-Level Medical Image Segmentation Network Based on Multi-Scale and Context Information Fusion Strategy," *IEEE Trans. Emerg. Top. Comput. Intell.*, vol. 8, no. 1, pp. 474-487, 2024.
- [15] H. Huang et al., "Combinatorial CNN-Transformer Learning with Manifold Constraints for Semi-supervised Medical Image Segmentation," in *Proceedings of the AAAI Conference on Artificial Intelligence*, vol. 38, no. 3, pp. 2330-2338, 2024.
- [16] T. Pin et al., "DA-DSUnet: Dual Attention-based Dense SU-net for automatic head-and-neck tumor segmentation in MRI images," *Neuro-computing*, vol. 435, pp. 103-113, 2021.
- [17] N. Shen et al., "SCANet: A Unified Semi-Supervised Learning Framework for Vessel Segmentation," *IEEE Trans. Med. Imaging*, vol. 42, no. 9, pp. 2476-2489, 2023.
- [18] O. Ronneberger et al., "U-Net: Convolutional Networks for Biomedical Image Segmentation," *Medical Image Computing and Computer-Assisted Intervention – MICCAI 2015*, pp. 234-241, 2015.
- [19] A. Vaswani et al., "Attention is All You Need," in *Proceedings of the 31st International Conference on Neural Information Processing Systems (NIPS 2017)*, pp. 6000-6010, 2017.
- [20] N. Wang et al., "MISSU: 3D Medical Image Segmentation via Self-Distilling TransUNet," *IEEE Trans. Med. Imaging*, vol. 42, no. 9, pp. 2740-2750, 2023.
- [21] J. Yang et al., "EPT-Net: Edge Perception Transformer for 3D Medical Image Segmentation," *IEEE Trans. Med. Imaging*, vol. 42, no. 11, pp. 3229-3243, 2023.
- [22] S. Jiang et al., "DPCFN: Dual path cross fusion network for medical image segmentation," *Eng. Appl. Artif. Intell.*, vol. 116, no. C, p. 105420, 2022.
- [23] J. Chen et al., "TransUNet: Transformers Make Strong Encoders for Medical Image Segmentation," arXiv preprint arXiv:2102.04306, 2021.
- [24] H. Cao et al., "Swin-Unet: Unet-Like Pure Transformer for Medical Image Segmentation," in *Computer Vision – ECCV 2022 Workshops: Tel Aviv, Israel, October 23–27, 2022, Proceedings, Part III*, pp. 205-218, 2023.
- [25] X. Huang et al., "MISSFormer: An Effective Transformer for 2D Medical Image Segmentation," *IEEE Trans. Med. Imaging*, vol. 42, no. 5, pp. 1484-1494, 2023.
- [26] H. Wang et al., "UCTransNet: Rethinking the Skip Connections in U-Net from a Channel-wise Perspective with Transformer," in *AAAI Conf. Artif. Intell.*, vol. 36, pp. 2441-2449, 2022.
- [27] D. Tan, R. Hao et al., "A Novel Skip-Connection Strategy by Fusing Spatial and Channel Wise Features for Multi-Region Medical Image Segmentation," *IEEE J. Biomed. Health Inform.*, vol. 28, no. 9, pp. 5396-5409, 2024.
- [28] Z. Zhou, M. M. R. Siddiquee, N. Tajbakhsh, and J. Liang, "UNet++: A Nested U-Net Architecture for Medical Image Segmentation," *Deep Learning in Medical Image Analysis and Multimodal Learning for Clinical Decision Support*, pp. 3-11, 2018.
- [29] H. Huang, Y. Wang, W. Lian, W. Zheng, and Q. Tian, "U-Net 3+: A full-scale connected U-net for medical image segmentation," *Pattern Recognition*, vol. 106, p. 107404, 2020.
- [30] A. Dosovitskiy et al., "An Image Is Worth 16 × 16 Words: Transformers for Image Recognition at Scale," in *Proc. Int. Conf. Learn. Represent.*, pp. 1-12, 2021.
- [31] M. Rahman et al., "Multi-scale Hierarchical Vision Transformer with Cascaded Attention Decoding for Medical Image Segmentation," in *Medical Imaging with Deep Learning*, vol. 227, pp. 1526-1544, 2024.
- [32] M. Rahman et al., "G-CASCADE: Efficient Cascaded Graph Convolutional Decoding for 2D Medical Image Segmentation," arXiv preprint arXiv:2310.16175, 2023.
- [33] M. Rahman et al., "Medical Image Segmentation via Cascaded Attention Decoding," in *2023 IEEE/CVF Winter Conference on Applications of Computer Vision (WACV)*, pp. 6211-6220, 2023.